Estimating the concentration of silver iodide needed to detect unambiguous signatures of glaciogenic cloud seeding

Jing Yang[1,2], Jiaojiao Li[1], Meilian Chen[1], Xiaoqin Jing[1,*], Yan Yin[1], Bart Geerts[3], Zhien Wang[4], Yubao Liu[1], Baojun Chen[2], Shaofeng Hua[2], Hao Hu[1], Xiaobo Dong[5], Ping Tian[6], Qian Chen[1], Yang Gao[2]

5   [1]Collaborative Innovation Center on Forecast and Evaluation of Meteorological Disasters (CIC-FEMD)/China Meteorological Administration Aerosol-Cloud and Precipitation Key Laboratory, Nanjing University of Information Science & Technology, Nanjing, 210044, China.
[2]China Meteorological Administration Key Laboratory of Cloud-Precipitation Physics and Weather Modification (CPML), Beijing, 100081, China.
10 [3]Department of Atmospheric Science, University of Wyoming, WY, 82071, USA.
[4]School of Marine and Atmospheric Sciences, Stony Brook University, NY, 11794, USA.
[5]Hebei Provincial Weather Modification Center, Shijiazhuang, 050021, China.
[6]Beijing Weather Modification Center, Beijing, 100089, China.

Correspondence to: Xiaoqin Jing (xiaoqin.jing@nuist.edu.cn)

15 **Abstract.** Detecting an unambiguous radar reflectivity signature is vital to investigate cloud seeding impacts. Radar reflectivity change attributed to seeding depends on both the cloud conditions and on the concentration of silver iodide (AgI) particles. In this study, the reflectivity change induced by glaciogenic seeding using different AgI particle concentrations is investigated under various cloud conditions, using a 1D ice growth model coupled with an AgI nucleation parameterization. In addition, an algorithm is developed to estimate the minimum AgI particle concentration needed for a measurable glaciogenic cloud seeding 20 signature. The results show that the 1D model captures the ice growth habit compared to available observations, and yields an unambiguous reflectivity change that is consistent with 3D model simulations and previous observational studies. Simulations indicate that seeding at a temperature of about -15 °C has the highest probability of detecting the radar seeding signature. This finding is consistent with the fact that the seeding temperature was about -15 °C or slightly warmer in most documented unambiguous seeding signature cases. Using the 1D model, 1000 numerical experiments are conducted, and the outputs are 25 used to develop a parameterization to estimate the AgI particle concentration that is needed to detect an unambiguous seeding signature. Application of this parameterization to a real case suggests that seeding between -21 °C and -11 °C can possibly produce unambiguous seeding signatures, and seeding at about -15 °C requires the least AgI particle concentration. Seeding at warmer temperatures in precipitating clouds requires an extremely high AgI amount and supercooled liquid water content. The results shown in this study deepen our understanding of the relationship between the AgI particle concentration and radar 30 seeding signature under different cloud conditions. The parameterization can be used in operational seeding decision making of the optimal amount of AgI dispersed.

1 Introduction

Glaciogenic seeding using dry ice or silver iodide (AgI) is the major technique to enhance precipitation in mixed-phase stratiform clouds (Rauber et al., 2019). The scientific principle is that plenty of supercooled liquid water exists in mixed-phase

35   clouds, while the concentration of natural ice nucleating particles is low, which limits the amount of liquid water that can be converted to precipitation naturally (Geerts and Rauber, 2022). Introducing more ice crystals through glaciogenic seeding can enhance the Wegener-Bergeron-Findeisen (WBF) process, which means the ice grows at the expense of liquid water, leading to more precipitating snow crystals (Jing et al., 2015). Investigating the seeding impact on clouds and precipitation has always been vital in this research field (Rasmussen et al., 2018; Rauber et al., 2019; Geerts and Rauber, 2022). However, the seeding

40   signature is often immersed in the large variability of natural precipitation. For decades, scientists have made great efforts to detect unambiguous seeding signatures in field measurements (e.g., French et al., 2018; Rauber et al., 2019; Wang et al., 2021; Zaremba et al. 2024).

The first unambiguous observational evidence of precipitation enhancement by cloud seeding is reported by Hobbs et al.,

45   (1981). In their study, dry ice was used to seed a nonprecipitating stratiform cloud. A Ka-band cloud radar showed a clear enhancement of radar reflectivity factor (Ze) after seeding, suggesting the formation of ice plumes. In 1990, Deshler et al. (1990) reported another case with evident precipitation enhancement based on radar measurement. Seeding produced echoes of 3-10 dBZ in nonprecipitating clouds. After that case study, unambiguous seeding signatures in stratiform clouds were rarely documented for more than 20 years, especially for the cases in which AgI was used; one exception is Huggins (2007), who

50   used a scanning Ka-band radar to depict the impact of ground-based AgI seeding. Similarly, Jing et al. (2015; 2016) and Jing and Geerts (2015) showed seeding effects based on X-band radar reflectivity data collected in the 2011-12 AgI Seeding Cloud Impact Investigation (ASCII, Geerts et al. 2013), but those studies analyzed the differences in composite radar reflectivity (SEED − NOSEED), rather than instantaneous reflectivity scans. Recently, in three cases from the 2017 Seeded and Natural Orographic Wintertime Clouds; The Idaho Experiment (SNOWIE; Tessendorf et al. 2019), an unambiguous airborne seeding

55   signature was detected using radar and airborne in-situ measurements. In all the three cases described in French et al. (2018) and Friedrich et al. (2021), the natural precipitation was weak, the ice concentrations in clouds were low (<1 L^{-1}), and seeding AgI near the cloud tops produced a significant enhancement of ice water content (IWC) and surface precipitation, and increase in reflectivity factor (Ze) of 10-30 dBZ after seeding, detected by a X-band radar. Enhancement of radar reflectivity of 10-30 dBZ induced by AgI seeding was also reported in the last few years from other regions (e.g., Dong et al., 2020; 2021; Yue et

60   al., 2021; Wang et al., 2021), and in some cases parts of the cloud regions were completely glaciated after seeding (Wang et al., 2024).

However, despite the successful case studies shown above, most field experiments failed to detect the seeding signature. For example, there were 18 intensive operation periods with airborne seeding in SNOWIE, but a clear seeding signature was

observed only in three of them (Geerts and Rauber, 2022). In general, airborne seeding of elevated layers of liquid water is more likely to be radar-detectable than ground-based seeding, because scanning radars cannot see impact very close to the ground, especially over complex terrain (beam blockage). In any event, most field measurements before SNOWIE showed no clear signatures of glaciogenic cloud seeding, though statistical analyses in randomized seeding experiments suggest precipitation enhancement by 3%-17%, and in some cases the precipitation enhancement is up to 57% (e.g., Geerts et al., 2013; Pokharel et al, 2014; Jing et al., 2015, Jing and Geerts, 2015, Jing et al., 2016). In these studies, the evidence in individual radar scans is insufficient to tell whether the seeding is ineffective, or the seeding signature is undetectable (Zaremba et al., 2024). We may conclude that the cloud conditions are not optimal or the AgI concentration is too low for producing a signature greater than the natural variability. The efficiency of cloud seeding depends on the cloud conditions. Previous studies suggest that for optimal seeding conditions, supercooled liquid water must be present in the cloud (Geerts and Rauber, 2022); the cloud depth above -5 °C should be deeper than 400 m for ice growth (Manton et al., 2011); the seeding temperature should be lower than -8 °C (Breed et al., 2014), and the concentrations of natural ice crystals should be low (Jing et al., 2016). However, the thermodynamic and microphysical conditions vary significantly in a cloud and differ substantially among different clouds. It is possible also that seeding is effective, but not radar-detectable, because the natural concentration of snow particles dominates the radar signal (Zaremba et al. 2024). Seeding under different conditions and using different AgI particle concentrations may result in different seeding signatures. It would be helpful in seeding operations if we can quickly estimate which region has the optimal seeding condition, and how much AgI is needed for an unambiguous seeding signature.

The purpose of this study is to develop an algorithm to estimate how much AgI is needed to detect the signature of glaciogenic cloud seeding. The basic idea is that Ze is determined by the ice crystal size and concentration, and the WBF process is the major ice growth mechanism in mixed-phase stratiform clouds. Since there are sophisticated theories and well-developed parameterizations for ice diffusional growth, we can model the Ze induced by cloud seeding. By conducting multiple sensitivity experiments with various cloud conditions, we can develop a parameterization that reveals the relationships between AgI particle concentration and the Ze induced by cloud seeding, and using this parameterization we can estimate the AgI particle concentration needed to produce a Ze greater than the natural variability. The algorithm and the results presented in this study can be used to improve cloud seeding operations efficiency.

The rest of the paper is organized as follows: Section 2 describes the ice nucleation and the ice growth model. The evaluation of the model, discussion of the model results, and the parameterization for AgI particle concentration is developed in Section 3. In Section 4, this parameterization is applied to a real case. The conclusions and discussion are presented in Section 5.

2 The ice nucleation and growth model

In this study, we use a one-dimensional (1D) model of ice nucleation and growth to simulate the growth trajectory of ice crystals. Similar models have been used in previous studies to investigate ice microphysics (Chen and Lamb, 1994; Korolev and Field, 2007) and to retrieve ice properties with radar measurements (Zhang et al., 2014). In addition, we implement an AgI nucleation parameterization (Xue et al., 2013a; 2013b) in the model to simulate the ice generation by cloud seeding. Using this model, we can estimate the IWC and Ze produced by cloud seeding in mixed-phase stratiform clouds with relatively weak turbulence.

2.1 Parameterization of AgI nucleation

To model the ice nucleation through AgI particles, we follow the parameterization described in Xue et al. (2013a). This parameterization is originally developed based on cloud chamber experiments from DeMott (1995) and Meyers et al. (1995). Four ice nucleation modes are considered. For *deposition nucleation*, which is valid when the saturation ratio with respect to ice greater than 1.04 and the temperature colder than 268.2 K, the fraction of AgI seeded that can nucleate ice is:

$$F_{dep} = a(S_i - 1) + b\left(\frac{273.16-T}{T_0}\right) + c(S_i - 1)^2 + d\left(\frac{273.16-T}{T_0}\right)^2 + e(S_i - 1)^3, \tag{1}$$

where $T_0 = 10$ K, $a = -3.25 \times 10^{-3}$, $b = 5.39 \times 10^{-5}$, $c = 4.35 \times 10^{-2}$, $d = 1.55 \times 10^{-4}$, and $e = -0.07$. S_i is the saturation ratio with respect to ice.

The fraction of AgI that can nucleate ice through *condensation-freezing nucleation*, which applies for temperature colder than 268.66 K, can be calculated using

$$F_{cdf} = a\left(\frac{268.66-T}{T_0}\right)^3 (S_w - 1)^2, \tag{2}$$

where $a = 900$. S_w is the saturation ratio with respect to water.

The third mode is *contact freezing*, which is minor compared to the other nucleation mechanisms:

$$F_{ctf} = F_{scav}[a + b(S_i - 1) + c(S_i - 1)^2 + d(S_i - 1)^3 + e(S_i - 1)^4 + f(S_i - 1)^5 + g(S_i - 1)^6], \tag{3}$$

where $a = 0.0878$, $b = 23.7947$, $c = 52.3167$, $d = 2255.4484$, $e = 568.3257$, $f = 2460.4234$, and $g = 263.1248$. F_{scav} is the fraction of the total AgI particles that are scavenged by cloud droplets (Caro et al., 2004). Contact freezing is valid for $S_i > 1.058$ and $T < 269.2\ K$.

And the last mode is *immersion-freezing*, which is valid for temperature colder than 268.2 K,

$$F_{imf} = aF_{imm}\left(\frac{268.2-T}{T_0}\right)^b, \tag{4}$$

where $a = 0.0274$, $b = 3.3$. F_{imm} is the fraction of AgI immersed in cloud droplets but not nucleated. Based on the equations
125 above, we can calculate the concentration of ice generated through cloud seeding given the AgI particle concentration. For
simplicity, this 1D model does not incorporate 3D turbulent dispersion of AgI particles.

2.2 Growth of ice crystals

In mixed-phase stratiform clouds with relative weak turbulence, the WBF process, where ice grows at the expense of liquid
130 water, is the most important mechanism for ice growth, so if there is sufficient liquid water in the cloud, the diffusional growth
contributes the most to ice mass and size. However, it should be noted that the WBF process is not always valid, if the updraft
is strong enough, the cloud will be supersaturated with respect to water, leading to simultaneous growth of droplets and ice
crystals. Korolev (2007) showed the WBF process only applies in downdrafts and weak updrafts, therefore, we emphasize that
the model used here only applies for stratiform clouds with weak turbulence. In fact, even weak turbulence may occasionally
135 result in supersaturation with respect to water, and radiative cooling near cloud top may also enhance the supersaturation.
These factors are not considered, and could in part contribute to the model uncertainties in the results shown in Section 3.

According to Mason (1953), the diffusional growth rate of an ice crystal is:

$$\frac{dm}{dt} = \frac{4\pi C(S_i - 1)f_v}{L_d^2/KR_vT_a^2 + 1/D_v\rho_s}, \tag{5}$$

140 where R_v is the specific gas constant for vapor, L_d is the latent heat of deposition, K is the thermal conductivity of air, T_a is
the ambient temperature, D_v is the diffusion coefficient of vapor, ρ_s is the density of saturated vapor, f_v is the ventilation
factor:

$$f_v = \begin{cases} 1 + 0.14X^2, & X < 1 \\ 0.86 + 0.28, & X \geq 1 \end{cases}, \tag{6}$$

where, $X = S_c^{1/3}R_e^{1/2}$, S_c is the Schmidt number, and R_e is the Reynolds number (Hall and Pruppacher, 1976).
145

In Eq. 5, the capacitance C reveals the shape of ice crystals, which is primary temperature-depended. There are many laboratory
experiments investigated the shapes of ice crystals during diffusional growth (e.g., Fukuta and Takahashi, 1999; Baikey and
Hallett, 2009). Typically, plate-like ice crystals (e.g., hexagonal plates, sectored plates, dendrites, etc.) form at temperatures
warmer than -4 °C, and at -8 °C – -22 °C; column-like ice crystals (columns, needles, etc.) form at temperatures between -4°C
150 and -8 °C (Fukuta and Takahashi, 1999). At temperatures colder than -22 °C, the ice crystals could be either columns or plates
(Baikey and Hallett, 2009). Based on laboratory experiments, Chen and Lamb (1994) developed a parametrization of C, for
plate-like ice crystals,

$$C = \frac{a\varepsilon}{\sin^{-1}\varepsilon}, \tag{7}$$

$$\varepsilon = \sqrt{1 - c^2/a^2} = \sqrt{1 - \phi^2}, \tag{8}$$

155   and for the column-like ice crystals, C is given by

$$C = \frac{c\varepsilon}{\ln[(1+\varepsilon)\phi]}, \tag{9}$$

$$\varepsilon = \sqrt{1 - a^2/c^2} = \sqrt{1 - \phi^{-2}}, \tag{10}$$

where a and c are the particle radius along the a-axis and c-axis. For plate-like ice crystals, the a-axis is longer than the c-axis, while for column-like particles, the c-axis is longer. $\phi = c/a$ is the aspect ratio of ice crystal. The change in the

160   surface volume of the ice crystal is expressed as:

$$dV = \frac{1}{\rho_{\text{dep}}} dm, \tag{11}$$

where ρ_{dep} is the mass density at the time of deposition. Chen and Lamb (1994) showed that $\rho_{\text{dep}}(\text{g } cm^{-3})$ can be expressed using:

$$\rho_{\text{dep}} = 0.91\exp\left[-3\frac{\max(\Delta\rho - 0.05, 0)}{\Gamma(T)}\right], \tag{12}$$

165    $\Delta\rho$ is the excess vapor density. $\Gamma(T)$ is the ice inherent growth ratio, which is determined based on laboratory experiments, and is related to the particle size (Chen and Lamb, 1994):

$$\Gamma(T) = \frac{dc}{\phi da}. \tag{13}$$

The initial ice particle is assumed to be spherical. The volume can be expressed as:

$$V = \frac{4}{3}\pi a^2 c = \frac{4}{3}\pi a^3 \phi, \tag{14}$$

170    $$d\ln V = 3d\ln a + d\ln\phi. \tag{15}$$

The differential representation of ϕ is:

$$d\phi = \frac{1}{a}dc - \frac{c}{a^2}da = \left(\frac{dc}{da} - \phi\right)d\ln a = \phi(\Gamma - 1)d\ln a, \tag{16}$$

$$\frac{d\phi}{\phi} = \frac{dV}{V}\left(\frac{\Gamma-1}{\Gamma+2}\right). \tag{17}$$

Based on the equations above, we can estimate the changes in ϕ, a and c with time:

175    $$\phi(t + \Delta t) = \phi(t)\left[\frac{V(t) + dV}{V(t)}\right]^{(\Gamma-1)(\Gamma+2)}, \tag{18}$$

$$a(t + \Delta t) = \left[\frac{3}{4\pi} \frac{V(t) + dV}{\phi(t + \Delta t)}\right]^{1/3}, \tag{19}$$

$$c(t + \Delta t) = \phi(t + \Delta t) \times a(t + \Delta t). \tag{20}$$

Although diffusional growth is the most important mechanism for ice growth in mixed-phase stratiform clouds,
accretional growth (riming) is also considered in the model. According to Heymsfield (1982), the mass growth rate
through riming can be parameterized as:

$$\frac{dm_R}{dt} = AV_t E(D, d)\text{LWC}, \tag{21}$$

where A is the particle cross-sectional area normal to the fall. V_t is the terminal velocity of ice crystals. LWC is the liquid
water content estimated by assuming adiabatic clouds. $E(D, d)$ is the collection efficiency between an ice crystal with
diameter of D, and a droplet with diameter of d. For simplicity, we assume a droplet diameter of 10 μm, which is a typical
size of droplets in continental clouds (Wallace and Hobbs, 2006; Wang et al., 2021).

To implement the impact of turbulence on the growth of ice crystals, we use a Gaussian normal distribution with a zero
mean vertical air velocity and standard deviations of 0.75 m s^{-1}. A similar method has been used in previous studies (e.g.,
Korolev et al., 2007; Zhang et al., 2014). The vertical velocity of an ice crystal is the summation of particle terminal
velocity and vertical air velocity.

2.3 Terminal velocity of ice crystals

The terminal velocity (or fall speed) of an ice crystal depends on its mass, size and habit, as well as the ambient air
density. In the present study, we follow the method developed by Heymsfield and Westbrook (2010) to estimate the
terminal velocity (V_t) of ice crystals, which has been evaluated against observations (Heymsfield and Westbrook 2010;
Zhang et al., 2014):

$$V_t = \frac{\eta R_e}{\rho_{\text{air}} D}, \tag{22}$$

where η is the dynamical viscosity and D is the maximum size of the projection of the particle perpendicular to the
direction of fall. According to Böhm (1992), $D = 2a$ for a plate, $D = 2\sqrt{ac}$ for column, and $D = 2r$ for a sphere. R_e is
the Reynolds number:

$$R_e = \frac{\delta_0^2}{4}\left(1 + \frac{4\sqrt{X^*}}{\delta_0^2\sqrt{C_0}}\right), \tag{23}$$

where $C_0 = 0.35$, $\delta_0 = 8.0$.

$$X^* = \frac{\rho_{\text{air}}}{\eta^2}\frac{8mg}{A_r^k}, \tag{24}$$

205 where the value of k is 0.5 according to Heymsfield and Westbrook (2010), A_r is the ratio of the projected area A of the particle to the area of the external circle:

$$A_r = A/[(\pi/4)D^2]. \tag{25}$$

Following Harrington et al. (2013), for plate-like particles:

$$A = \pi a^2 (\rho_i/\rho_{bi})^2, \tag{26}$$

210 and for columnar particles:

$$A = \pi a c, \tag{27}$$

where ρ_i is the density of ice crystal, ρ_{bi} is the bulk density of solid ice (= $0.91 g\ cm^{-3}$). The ice shape (plate-like or column-like) is assumed not changing with height as it falls.

215 **2.4 Calculation of IWC and Ze**

In this model, we assumed the initial ice size distribution follows the modified gamma distribution (Mace et al., 1998):

$$N_i(D) = N_X \exp{(\alpha)}(\frac{D}{D_X})\exp{(-\frac{D\alpha}{D_X})}, \tag{28}$$

where $D_X = 10$ μm, and $\alpha = 2$. N_i is the ice concentration per unit of length, N_X is the number concentration per unit of length at the functional maximum, and is determined by the ice nucleation by AgI. This initial size distribution is partitioned to 80

220 bins with isometric radius intervals, and we loop through all the bins to simulate the growth of ice crystals with different initial sizes. Based on the modelled ice mass and size, we can calculate the IWC and Z_e:

$$\text{IWC} = \int_0^\infty m(D)N_i(D)\,dD, \tag{29}$$

$$Z_e = N_i \int_0^\infty f(D_m){D_m}^6\,dD, \tag{30}$$

where, D_m is the melted ice diameter, $f(D_m)$ is the normalized ice size distribution, N_i is the ice concentration.

225

In turbulent clouds, the ice crystals may disperse horizontally with time, resulting in a reduced ice concentration. In 1D model, we can estimate the change in $N_i(D)$ by solving the 1D dispersion equation:

$$\frac{\partial N_i}{\partial t} = v\frac{\partial^2 N_i}{\partial x^2}, \tag{31}$$

where ν is the turbulent kinematic diffusion coefficient and depends on the turbulent intensity. In mixed-phase stratiform
230   clouds with relatively simple dynamics, ν is typically smaller than 10 m s^{-2} (Pinsky et al., 2018). In clouds with strong wind
shear or embedded convections, ν could be larger, and the ice growth trajectory could be much more complicated. Therefore,
we emphasize again that the model described here only applies to stratiform clouds with relatively weak turbulence. In the
present study, the value of ν is randomly selected between 1 and 10 m s^{-2}. In clouds with strong turbulence or embedded
convection, the microphysics and dynamics are much more complicated (Yang et al., 2016a, 2016b).

235   **3 Model results**

3.1 Examples of ice microphysics from the 1D model

First, we evaluate the growth of a single ice crystal simulated using the 1D model. Figure 1 compares the modelled mass and
size of a single ice crystal with the laboratory experiments from Takahashi et al. (1991). The laboratory experiments were
conducted at various temperatures under a standard atmospheric pressure. The initial ice crystal is assumed spherical and has
240   a radius of approximately 4 μm. In the model simulation, we use the same thermodynamic conditions and initial size of ice
(Eq. 28 is used other than Fig. 1) as the laboratory experiments. It is seen from the figure that the modelled results are fairly
consistent with the observations. The mass growth rate has two peaks, at -15 °C and -6 °C, and is the highest at -15 °C. The
ice crystal forms at -15 °C is plate-like, and that forms at -6 °C is column-like (Section 2.2, Eq. 7-10). After 25 minutes, the
mass of ice crystal grows at -15 °C is about an order of magnitude higher than that grows at -20 °C. The sizes at different axes
245   depend on the shape of ice crystals. At -6 °C, the ice crystal is column-like, so the c-axis is the largest, while at -15 °C, the a-
axis is the largest as the ice crystal is plate-like. The ice size can rapidly increase from 4 μm to more than 1 mm within 20
minutes at -15 °C and -6 °C. At temperatures lower than -20 °C, the ice growth habit is less sensitive to the temperature. In
general, the uncertainty of modelled ice mass and size is less than 20% compared to the observation. This gives us the
confidence needed to use the model to estimate the ice growth.
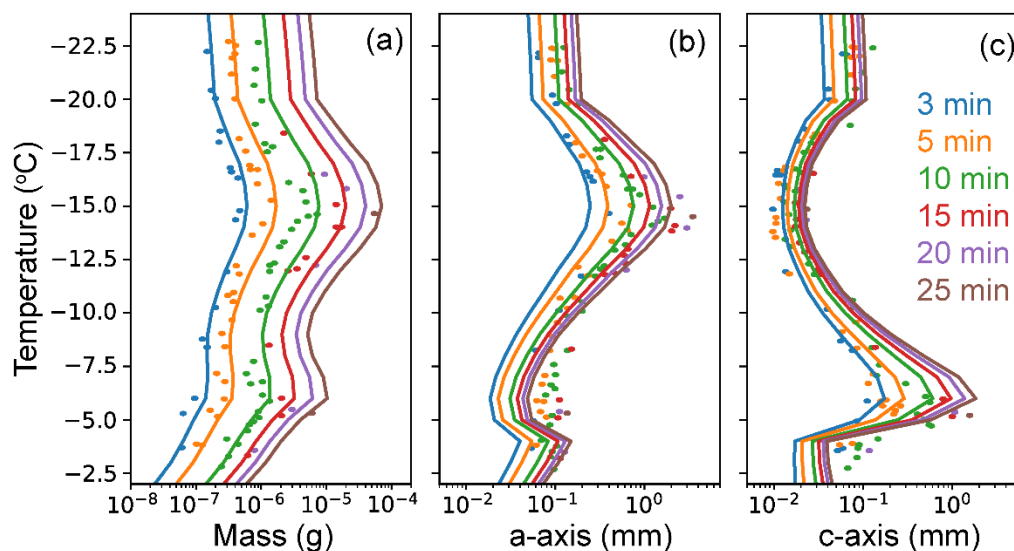
250

Figure 1. (a) Growth of the mass of a single ice crystal as a function of time at different temperatures under a standard atmospheric pressure. The dots are from laboratory experiments conducted by Takahashi et al. (1991) and the curves are from model simulations. (b) and (c) are similar to (a) but for the *a*-axis and *c*-axis, respectively.

255 According to Figure 1, it is expected that a detectable seeding signature is more probable at -15 °C or colder temperatures. For investigating the seeding signature at a given height, it is necessary to explore how the IWC and Ze change vertically as the ice crystals fall from the seeding level. Figure 2 shows the vertical profiles of IWC and Ze for a seeding temperature of -15 °C, -19 °C, and -22 °C (at a height of 5 km, 5.6 km, and 6.1 km, respectively). The results are obtained based on 10 numerical experiments for each seeding temperature. The shaded area indicates the 25th-75th percentiles and the solid lines are the mean

260 profiles. The uncertainties are due to the random numbers used in modelling the turbulence effect. Seeding at a relatively low temperature results in a higher ice concentration. On average, for an AgI particle concentration of 350 cm^{-3}, the ice concentration is 2.8 L^{-1}, 3.7 L^{-1}, and 4.5 L^{-1} for the seeding temperature of -15 °C, -19 °C, and -22 °C, respectively. For an AgI particle concentration of 35 cm^{-3}, the ice concentrations are 10 times lower. Regardless of the concentration of AgI particles, it is seen that the vertical variations of IWC and Ze are consistent. Below 4.7 km, IWC and Ze are the greatest when the seeding

265 temperature is -15 °C, and are the lowest when the seeding temperature is -22 °C. Although more ice can be nucleated through AgI at a lower temperature, their mass growth is much slower than the ice initiated at -15 °C, leading to lower IWC and Ze, which are more sensitive to size than concentration. The vertical variations of IWC and Ze are also related to the terminal velocity of ice crystals with different shapes. Ice crystals initiated at -22 °C have a similar scale along the *a*-axis and *c*-axis, thus the ice particle is more spherical compared to the plate-like ice initiated at -15 °C. The plate-like ice crystals have a small

270 terminal velocity, so they can stay at temperatures near -15 °C for a relatively long time, resulting in a substantial increase in ice mass and size. However, the ice particles initiated at -22 °C have a larger terminal velocity when they fall into the -15 °C

level. Long-term remote sensing measurements also indicate the average Ze in the cloud layer is the highest when the cloud top temperature is -15 °C (Zhang et al. 2014). Based on the results shown in Figures 1 and 2, it is suggested that seeding at a temperature of -15 °C can give a higher probability of detecting the seeding signature using radar. This conclusion is

275   interestingly consistent with the fact that the seeding temperature was about -15 °C (or slightly warmer in nonprecipitating clouds) in many of the cases with unambiguous seeding signatures detected (e.g., French et al., 2018; Yue et al., 2022; Wang et al., 2024), while at colder or warmer seeding temperatures in precipitating clouds, no clear seeding signature was observed.
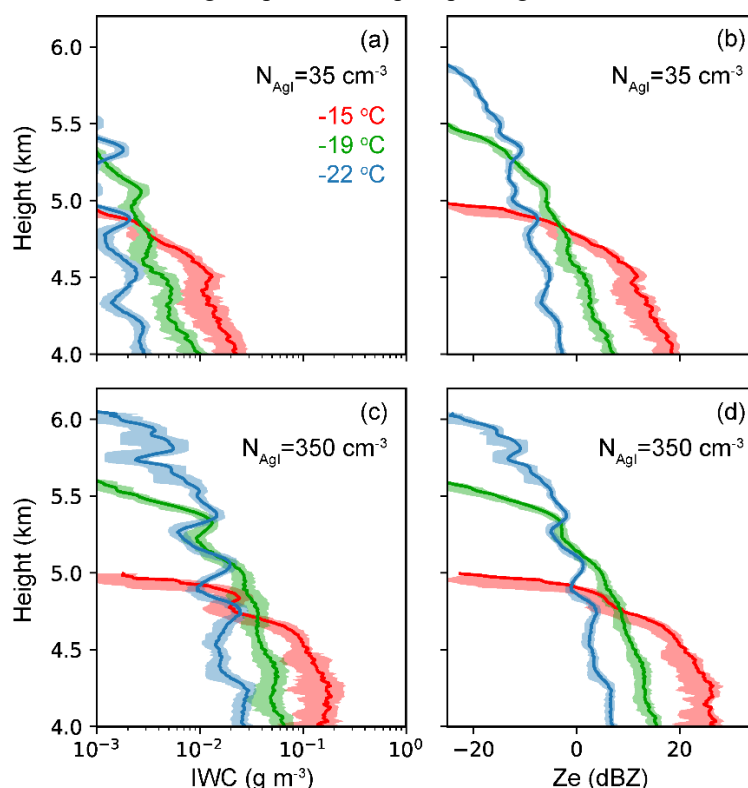
Figure 2. Vertical profiles of (a and c) IWC and (b and d) Ze from the simulations with different seeding temperatures
280   **and an AgI particle concentration of (a and b) 35 cm⁻³, and (c and d) 350 cm⁻³. The results are obtained based on 10 numerical experiments for each seeding temperature. The shaded area captures the 20ᵗʰ-80ᵗʰ percentile range, and the solid lines are the mean profiles.**

3.2 Comparison to 3D model simulation

285   To further evaluate the 1D growth model, it is compared with the 3D large eddy simulation (LES) of a shallow stratiform cloud. The cloud was observed on 1 January 2022 in Northern China. The cloud depth was approximately 600 m, and the cloud top temperature was approximately -16 °C (Wang et al., 2024). This cloud was seeded near -15 °C, and evident Ze

enhancement was detected by radar after seeding (Wang et al., 2024). The cloud was almost all liquid before seeding, the seeded area quickly glaciated within an hour. More details of measurements can be found in Wang et al. (2024). In this study,

290 we use the LES mode in WRF with periodic boundaries to simulate the cloud. Figure 3 shows the initial profiles of temperature, potential temperature, vapor mixing ratio, and wind velocity. Adiabatic liquid water content is assumed in the cloud (shaded area in Fig. 3b), and the wind shear in the cloud layer is relatively weak (Fig. 3c). The model has a horizontal resolution of 50 m, and the domain size is 10 km × 10 km × 4 km. 120 vertical levels are used to resolve the vertical structure of the cloud. A ±0.1 K temperature perturbation is added at the cloud base to kick off turbulence. A spin-up time of 30 min is used (Yang et

295 al., 2024), and the ice process is turned off during the spin-up time. Seeding is conducted at 30 minutes along a straight line perpendicular to the wind at -15 °C. We tested two different AgI particle concentrations (35 cm^{-3} and 350 cm^{-3}) in the simulations. The physics schemes used in the simulation include the Revised MM5 surface layer scheme (Jiménez et al., 2012), the Noah Land Surface Model (Tewari et al., 2004), the Rapid Radiative Transfer Model (Mlawer et al., 1997), and the fast spectral bin microphysics scheme (Khain et al., 2004), which can explicitly simulate more complicated microphysics than the

300 1D model. Cumulus and boundary layer parameterizations are turned off in the LES. The cloud condensation nuclei (CCN) concentration is expressed by $N_{CCN} = N_0 S_w{}^k$, N_0 refers to the CCN concentration at a supersaturation level of 1%, S_w represents the supersaturation with respect to water (%), k is the slope of the CCN size distribution. For continental China, Qu et al. (2017) suggested N_0 = 4000 and k = 0.9. The warm rain process is not possible with such a high aerosol concentration and weak wind shear in the cloud, since collision-coalescence cannot be kickstarted. Since the observation suggests the cloud

305 is all liquid before seeding, the natural ice nucleation process is turned off in the model. Thus, ice crystals are only generated due to cloud seeding. Similar to the 1D model, the AgI nucleation parameterization is from Xue et al. (2013a).
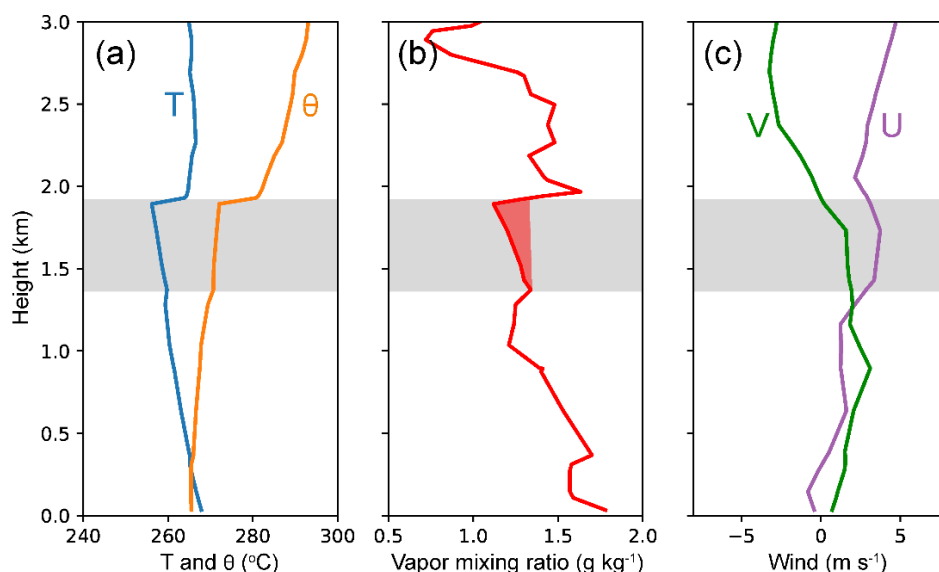
Figure 3. The initial profiles of (a) temperature and potential temperature, (b) vapor mixing ratio, and (c) U and V components of the wind field. The shaded area in (b) indicates the initial liquid water mixing ratio.

310

Figure 4 shows the cloud water and ice mixing ratio 20 (and 30) minutes after seeding in the 3D LES model. Ice crystals, which are initially nucleated near the cloud top, can rapidly grow and fall out of the cloud within 30 minutes. With a lower AgI concentration (35 cm^{-3}), the ice mixing ratio is lower than 0.06 g kg^{-1} after 30 minutes, while with a higher AgI particle concentration (350 cm^{-3}), the modeled ice mixing ratio exceeds 0.15 g kg^{-1}. Since the cloud is all liquid in areas unaffected by

315   seeding, the seeding signature can be well identified once the ice plume forms, either using in-situ measurements or remote sensing measurements (Wang et al., 2024; French et al., 2018).

A higher ice mixing ratio implies a higher radar reflectivity. As shown in Figure 5, with a lower AgI particle concentration (35 cm^{-3}), the maximum Ze near the cloud base 30 minutes after seeding is approximately 13 dBZ, while for a higher AgI particle

320   concentration, the Ze exceeds 20 dBZ (350 cm^{-3}). The Ze is relatively small near the cloud top and increases from cloud top to base. Below the cloud base, Ze decreases due to ice sublimation. The magnitude of Ze in the core of seeding plumes (5-30 dBZ) is fairly consistent with observational studies in which cloud seeding is operated at -15 °C (Wang et al., 2021; French et al., 2018), indicating the LES model can capture the characteristics of ice growth habit. The ice concentration in such a shallow cloud with top temperatures warmer than -15 °C is typically low (Zhang et al., 2014), resulting in a weak Ze in the natural

325   cloud. The Ze attributed to cloud seeding (Fig. 5) is sufficiently large to be detected by operational weather radars.
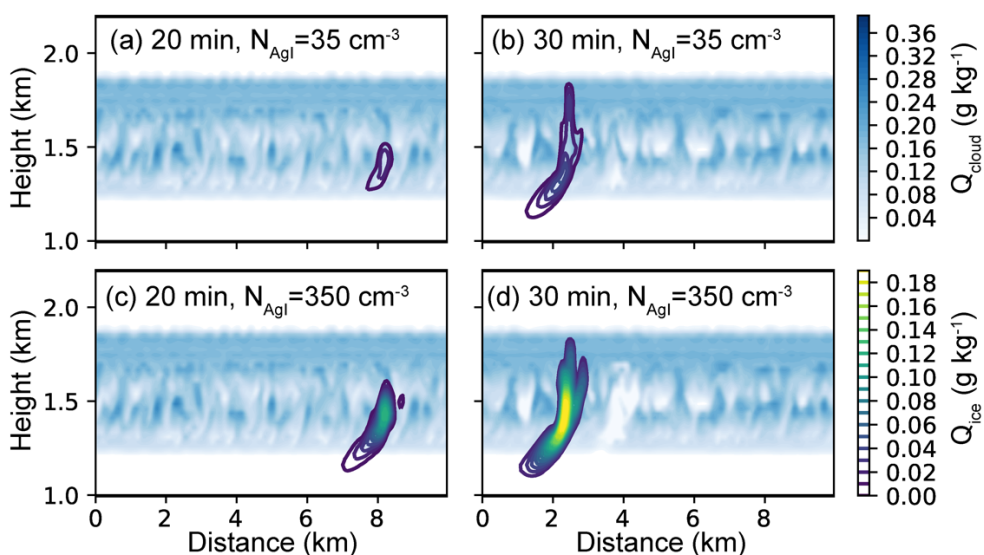
Figure 4. Cross sections of liquid water mixing ratio (blue shading) and ice mixing ratio (colour contoured) from the 3D LES model. (a and b) 20 and 30 minutes after seeding with an AgI particle concentration of 35 cm^{-3}, (c and d) similar to (a) and (b) but for an AgI particle concentration of 350 cm^{-3}.
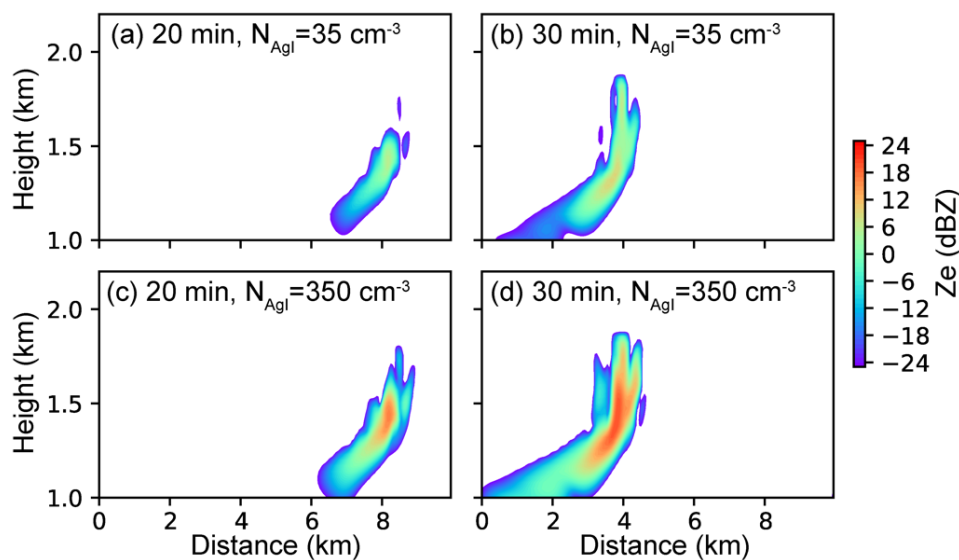
330

Figure 5. Cross sections of Ze from the 3D LES model. (a and b) 20 and 30 minutes after seeding with an AgI concentration of 35 cm⁻³, (c and d) similar to (a) and (b) but for an AgI particle concentration of 350 cm⁻³.

Figure 6 compares the radar reflectivity from the 1D model and 3D model simulations. The left and right boundaries of the

335   blue shaded area indicate the 95th percentile and the maximum Ze respectively from the 3D model. As shown in the figure, within a depth of 300 m from the seeding level, the maximum radar reflectivity from the 1D model is underestimated compared to the 3D model, probably because of the oversimplified cloud dynamics. In real clouds, there are updrafts induced by turbulent eddies, which can lift some of the ice crystals to relatively high levels, this is not fully considered in the 1D model. In the 3D simulation, we can see the Ze near cloud top is larger at 30 min than at 20 min, reflecting vertical mixing when ice crystals are

340   small (Fig. 5). Below 1.5 km, the 1D model is generally consistent with the 3D model, suggesting the microphysics of ice growth dominate the Ze profiles at these levels, and the oversimplified dynamics do not change the magnitude of Ze. The slight underestimation may be in part because ice aggregation is not considered in the 1D model. Near the cloud base, an AgI concentration of 35 cm⁻³ leads to a maximum reflectivity of 13 dBZ (Fig. 6a), and the Ze increases to 22 dBZ as the AgI concentration increases to 350 cm⁻³ (Fig. 6b). This magnitude is similar for the 1D and 3D model. Therefore, the 1D model is

345   valid for investigating the vertical variation of Ze more than 300 m below the seeding level. For the Ze near the seeding level, the 1D model is probably not reliable. In the following analysis the target level (defined as the level where we want to detect unambiguous seeding signatures) has to be more than 300 m below the seeding level.
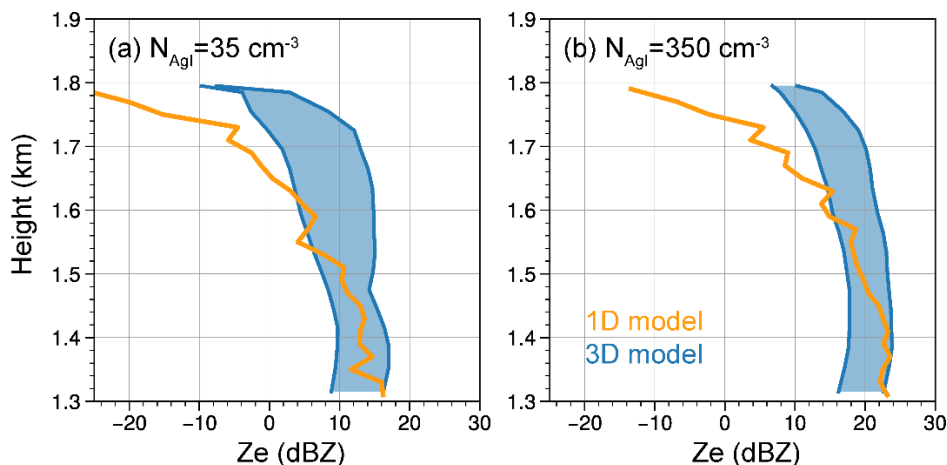
Figure 6. The vertical profiles of Ze simulated using the 1D and 3D models with an AgI particle concentration of (a) 35
cm⁻³, and (b) 350 cm⁻³, respectively. The left and right boundaries of the blue shaded area indicate the 95ᵗʰ percentile
and the maximum Ze from the 3D model, respectively.

3.3 Parameterizing the AgI concentration needed to detect unambiguous seeding signatures

Since the 1D model can simulate the growth habit of ice crystals reasonably well, we conducted 1000 numerical experiments with a variety of different seeding temperatures (-30 °C – -7 °C), seeding pressures (350 hPa – 850 hPa), AgI particle concentrations ($1 \ cm^{-3}$ – $10^{6} \ cm^{-3}$), and depths from seeding level (i.e., the vertical distances between the seeding levels and target levels, 500 m – 4000 m). We include very high AgI particle concentration in the experiments because it is helpful to have a large parameter space to constrain the parameterization. In addition, in many observational studies, normal AgI particle concentration ($10–1000 \ cm^{-3}$) is insufficient to detect the seeding signature, though AgI particle concentration with a magnitude of $10^{5} – 10^{6} \ cm^{-3}$ is probably not possible in reality. Again, it should be noted that we assume there is sufficient supercooled liquid water in the cloud, however, this is not always true. The liquid water amount needed to support the growth of ice will be discussed later. Figure 7 shows the modeled Ze (colored) at the target levels as a function of different seeding temperatures, AgI particle concentrations, and depth from the seeding level. Statistically, we can see the temperature and AgI particle concentration both have important impacts on the seeding impacts. The modeled Ze is relatively high at -15 °C with a higher AgI particle concentration. Clouds with cold top temperatures can be either shallow or deep, for a given seeding temperature, the modeled Ze increases with the increasing depth (similar to the Ze profiles in Fig. 2). Cloud top pressure also influences the growth rate of ice crystals but its impact is minor compared to the other factors.
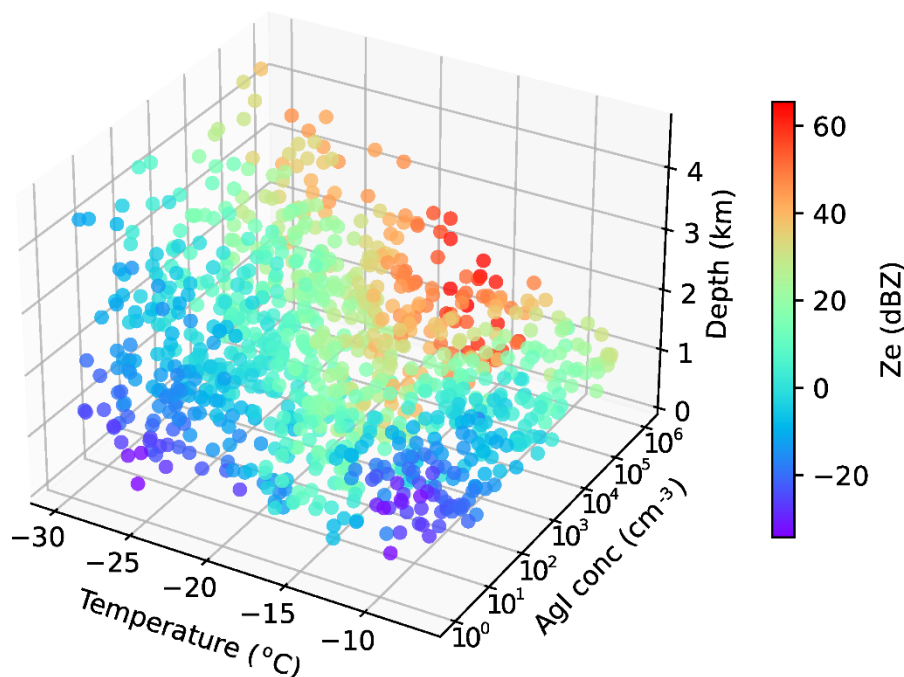
Figure 7. The modeled Ze (colored dots) at target levels for different seeding temperatures, AgI concentrations, and
370 **cloud depth from the seeding level based on the data from 1000 numerical experiments using the 1D model.**

Using the results from the 1000 numerical experiments, we parameterize the AgI particle concentration that is needed to detect
the seeding signature. We train the data using a polynomial regression, the inputs are seeding-level temperature (T_{seed}),
pressure (P_{seed}), cloud depth from the seeding level (D_{seed}), and Ze attributed to seeding at the target level (Z_{e_target}). The
375 output is AgI particle concentration (N_{AgI}) at the seeding level.

$$N_{AgI} = f(T_{seed}, P_{seed}, D_{seed}, Z_{e\_target}) \tag{32}$$

Thus, for a given cloud, we can decide how much AgI is needed to seed at different heights to produce a radar signal exceeding
the natural variability at the target level. Figure 8a compares the modeled and parameterized AgI particle concentration.
Generally, the data points are along the 1:1 line, indicating that the parameterization can reasonably reveal the relationships
380 between AgI particle concentration and Ze for different cloud conditions. In the polynomial regression used for Fig. 8a, 6
degrees (i.e., the maximum power for the input variables) are used. We also tried different values of degree in the regression,
as shown in Fig. 8b, a degree of 6 gives the smallest root-mean-square-error (RMSE) and the highest correlation coefficient
between the modeled and parameterized AgI particle concentration. The correlation coefficient increases as the degree
increases from 1 to 6. For degrees larger than 6, the polynomial regression becomes overfitted. 1000 numerical experiments
385 are sufficient to generate a statistically robust result, because fitting the data using slightly less experiments (800-999) gives
similar results (not shown).
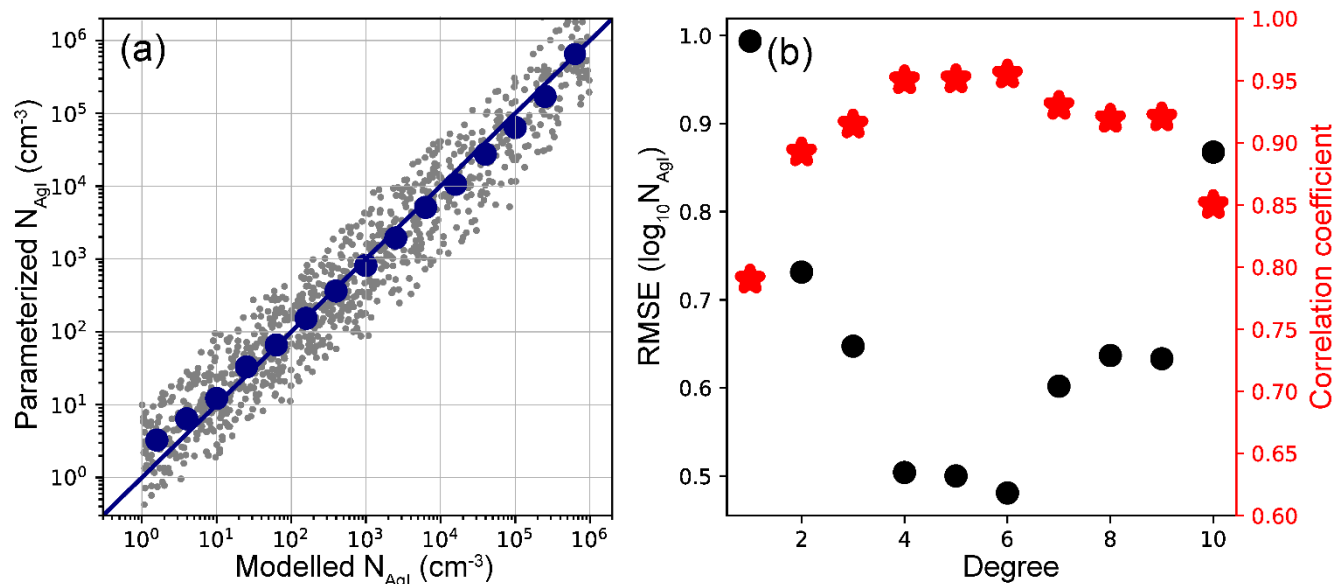
Figure 8. (a) Scatter plot of the parameterized and modelled AgI particle concentration. The grey dots are the results from the 1000 numerical experiments, and the dark blue dots are binned averages. The parameterization is developed using the polynomial regression with a degree of 6. (b) RMSE and correlation coefficient between the parameterized and modelled AgI concentration for different polynomial degrees used in the regression.

4 Application to a real case

4.1 Radar observations

In this section, the parameterization is applied to a mixed-phase stratiform cloud with moderate natural precipitation (0.2-0.3 mm h^{-1}). The purpose is to estimate the concentration of AgI that is needed to detect the seeding signature in this case. Figure 9 shows the temperature profile and the Ze measured by a Ka-band cloud radar. The cloud was observed in the Hulun Buir region in the northeast of China on 3 August 2023. It formed during the passage of a warm front (near z=1.7 km in Fig. 9a). The cloud was stratiform and deep, with a top temperature of about -25 °C. The freezing level was at about 4.2 km. It is seen that there are large natural variabilities of the observed Ze. Above the freezing level, the largest Ze is about 15 dBZ, and the average Ze is 4 dBZ.
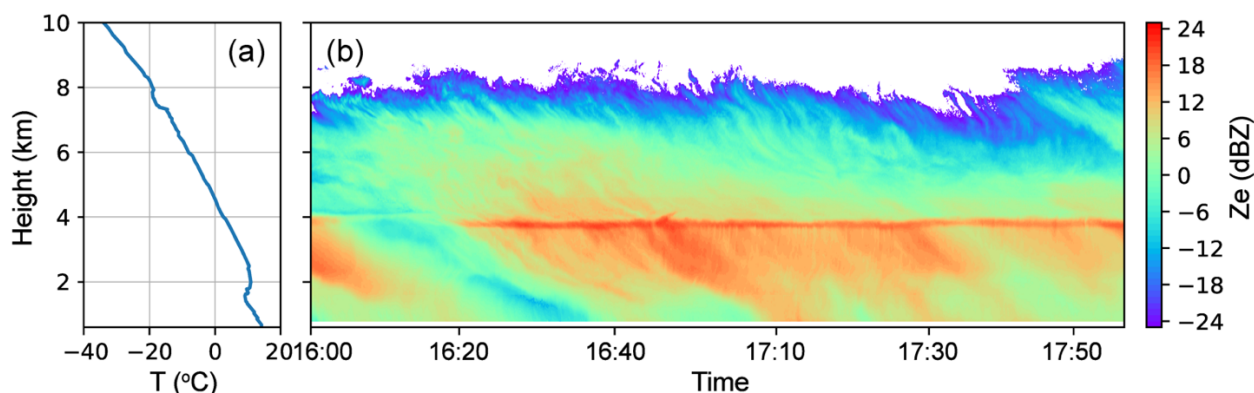
Figure 9. (a) Temperature profile measured by radiosonde and (b) Ze measured by a Ka-band cloud radar for a stratiform cloud observed in the Hulun Buir region in the northeast of China on 3 August 2023.

405 To determine the AgI particle concentration, firstly we need to choose a threshold of Ze induced by cloud seeding, i.e., the seeding-induced Ze should be higher than this threshold thus the composite Ze (natural and seeding) can exceed the natural variability after seeding. Figure 10 shows the contoured frequency-by-altitude diagram (CFAD) of observed Ze, the solid red line indicates the average Ze plus one standard deviation, and the dashed line indicates the mean plus 2 standard deviations. These two thresholds are probably still not large enough if the seeding is performed in regions with relatively high natural Ze

410 (e.g, at 16:40), but may be fine if the seeding is conducted at 16:10 when the natural Ze is low. To better detect the seeding signature, a larger value of Ze is necessary, such as the mean plus 3 standard deviations (dotted line), which well exceeds the maximum natural Ze.
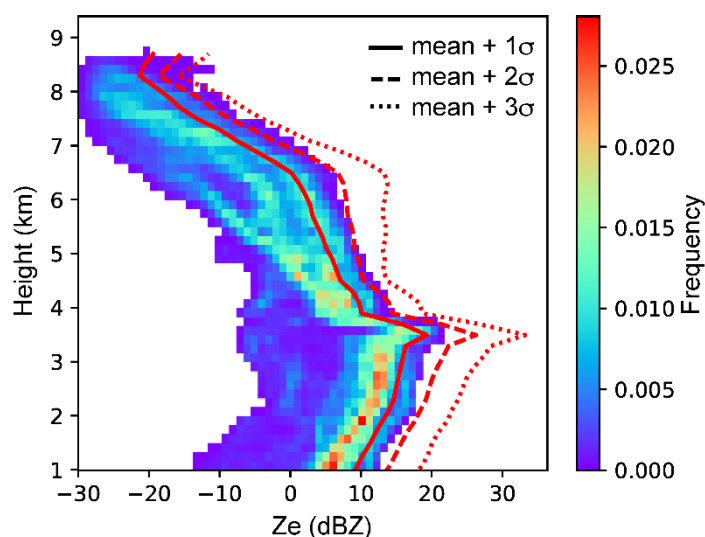
Figure 10. CFAD of Ze observed by the Ka-band radar for the period shown in Fig. 9b. The solid, dashed, and dotted

415 **lines indicate the mean Ze plus 1, 2 and 3 standard deviations, respectively.**

4.2 AgI concentration needed to detect the seeding signature

Figure 11 shows the AgI particle concentration that is needed at different heights (-22 °C - -7 °C) to detect the Ze attributed to seeding above the freezing level (4.2 km). We test three different thresholds for seeding-induced Ze (5.9 dBZ, 11.2 dBZ, and

420   16.7 dBZ). These values correspond to a composite Ze (mean natural Ze and seeding Ze) of 8 dBZ, 12 dBZ, and 17 dBZ above the freezing level (see the three red lines in Fig, 10). It is within the expectation that more AgI is needed to obtain a larger Ze, but the vertical variations of the three profiles of AgI particle concentration are very similar (Fig. 11). The required AgI concentration is the lowest at about 7.3 km (-15 °C), where 20 cm^{-3} AgI is sufficient for the cloud seeding to induce a composite Ze exceeding 17 dBZ. Therefore, seeding at this level provides the highest probability of detecting the seeding signature.

425   However, airborne seeding at -15 °C is not always possible because of flight limitations (e.g., airframe icing). Seeding at colder or warmer temperatures may also exceed the Ze threshold if the AgI particle concentration is high enough, however, since a normal AgI concentration in cloud seeding operation has a magnitude of 10-1000 cm^{-3}, it is unlikely that seeding below 6.5 km will yield a detectable seeding signal near the freezing level in this case.
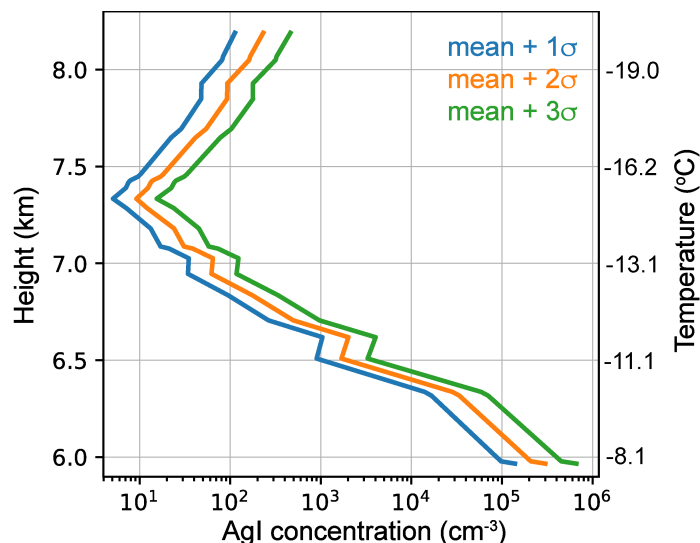
430   **Figure 11. The profiles of AgI concentration needed to detect the seeding signature at the freezing level for different Ze anomaly thresholds.**

An important assumption in the parameterization is that sufficient supercooled liquid water exists for the ice growth. However, this assumption is not always valid, especially when the natural ice concentration is high. Figure 12 shows the liquid water

435   path (LWP) between the seeding level and the target level (4.2 km), needed to support the growth of ice for different seeding temperatures. Seeding at -15 °C consumes the least liquid water, which is about 50 g m^{-2}. The LWP in this cloud observed by

a microwave radiometer is mostly larger than 300 g m⁻², though supercooled water only accounts for part of the total LWP as there was rain water, it is expected that there is sufficient water for the ice growth if seeding at a temperature of -19 °C – -13 °C. Seeding at a slightly warmer or colder temperature (-11 °C and -21 °C) may also produce unambiguous signatures if there is sufficient supercooled liquid water. Seeding at temperatures warmer than -10 °C requires much more liquid water due to the high AgI particle concentration, therefore, the size of ice crystals and Ze may be even smaller as suggested by the model. Previous observational studies suggest the LWP in shallow mixed-phase stratiform clouds is often lower than 100 g m⁻² (Zhang et al., 2014). Such a low LWP prevents the growth of ice crystals if the ice concentration is high. In addition, if there is no continuous supply of liquid water (e.g., in orographic updrafts), seeding can cause complete cloud glaciation in the seeded region (Dong et al. 2021).
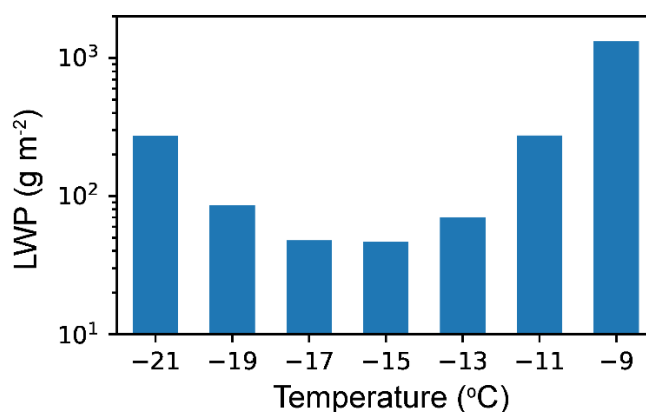
Figure 12. The LWP needed to support the growth of ice for different seeding temperatures between the seeding level and the target level.

5 Discussion and Conclusions

In this study, the IWC and Ze induced by glaciogenic seeding using different AgI particle concentrations under various cloud conditions are investigated using a 1D ice growth model coupled with an AgI nucleation parameterization. In addition, an algorithm is developed to estimate the AgI particle concentration that is needed to detect the signature of glaciogenic cloud seeding. This algorithm, which is a parameterization that links the AgI particle concentration to the radar Ze induced by seeding, is developed based on multiple numerical experiments using the 1D model. The main conclusions are as follows:

(1) The 1D model captures characteristics of the ice growth habit compared to observations. At cloud depths exceeding 300 m from the seeding level, the modelled IWC and Ze is consistent with the 3D LES model, while within a depth of 300 m, the 1D model underestimates the IWC and Ze.

460 (2) Since ice crystals have the largest growth rate at -15 °C, the IWC and Ze induced by cloud seeding at -15 °C is larger than
         seeding at colder temperatures. Therefore, a radar seeding signature is most likely to be detected at a temperature of about
         -15 °C. This finding is consistent with the fact that the seeding temperature was about -15 °C or slightly warmer in most
         documented unambiguous seeding signature cases.

465 (3) A higher AgI particle concentration leads to higher Ze *ceteris paribus*. Both the 1D and 3D models suggest that for an
         AgI particle concentration of 35 cm^{-3}, the Ze induced by cloud seeding is 10-20 dBZ, and for an AgI particle concentration
         of 350 cm^{-3}, the Ze is 20-30 dBZ, as long as sufficient liquid water is available.

     (4) Using the 1D model, 1000 numerical experiments were conducted for various cloud conditions and AgI particle
470   concentrations. Statistical analysis based on the model data indicates AgI particle concentration and temperature are the
         major factors controlling the IWC and Ze at the target level. The depth from the seeding level also influences the IWC
         and Ze as a deeper cloud provides a longer path for ice growth.

     (5) Based on the data from the 1000 numerical experiments, a parameterization is developed using polynomial regression to
475   estimate the minimum AgI particle concentration that is needed to detect the signature of glaciogenic cloud seeding. The
         seeding temperature, pressure, Ze, and cloud depth from the seeding level are used as the inputs to train the
         parameterization, and the AgI particle concentration is the output.

     (6) Application of this parameterization to a real case with natural precipitation suggests seeding at about -15 °C requires the
480   least AgI to obtain a seeding signature exceeding the natural variability. Seeding at slightly colder or warmer temperatures
         also may produce a detectable signature, but requires more AgI and supercooled liquid water. Seeding impact at
         temperatures warmer than -10 °C is unlikely to be detected in this case, because it requires an extremely high concentration
         of AgI and an LWP exceeding 1000 g m^{-2}. However, for nonprecipitating clouds, seeding at temperatures warmer than -
         10 °C may produce detectable seeding signature.

485

This study has several limitations:
-    The results shown here only apply to mixed-phase stratiform clouds with relatively simple dynamics, because we assumed
     a relatively weak turbulence in the model. In clouds with stronger turbulence or convections, the ice growth trajectories
     are more complicated, thus, a 3D model has to be used to investigate the seeding-induced signature under various ambient
490 conditions (Xue et al., 2022; Hua et al., 2024).
-    AgI released pyrotechnically from point sources on the ground or in the air (burn-in-place or ejectable flares, rockets …)
     vary vastly in concentration. In fact, AgI particle concentrations in 3D models typically are depicted on a log scale rather

than a linear scale (e.g., Xue et al. 2013b; 2022). Therefore, seeding operators have little control over AgI concentrations. But as AgI disperses from a point source in boundary layer or cloud turbulence, our study shows that it may cross a

495   "sweet spot" where, under given cloud conditions, the seeding impact is optimally detectable.

- The parameterization developed in this study applies to airborne cloud seeding. For ground-based seeding, which is often used for orographic clouds, the AgI particles are mixed into clouds mainly through boundary layer turbulence. Boundary layer convection and hydraulic jump in the lee may enhance the vertical dispersion of AgI particles (Jing et al., 2016). Therefore, to investigate the ice nucleation and growth, it is important to resolve the vertical dispersion of AgI particles

500   (Xue et al., 2013b), which is not considered in the 1D model presented in this study. High-resolution LES model is the better choice to model the impact of ground-based cloud seeding (Xue et al., 2013b; Chu et al., 2014).

- In the present study, the Ze is calculated assuming the Rayleigh scattering, thus the radar signal is more sensitive to the size of particles. For radars with shorter wavelengths, such as the W-band cloud radar, the signal could be sensitive to the ice concentration. In the SNOWIE experiment, both W-band radar and X-band radars were used. The W-band radar

505   saw clear Ze enhancement near the seeding level, while for the X-band radar, the Ze in the ice plume was weak near the seeding level, and increased downwind towards the surface (Friedrich et al. 2021). This is consistent with the model results shown in this study. Unfortunately, the 1D model poorly represents the ice microphysics near the seeding level (Fig. 6), so it cannot be used to develop a similar parameterization for W-band radar.

- In our study, it is expected that cloud seeding contributes the majority of ice mass in the seeding plume. The best radar

510   seeding signatures come from clouds with no or very weak natural precipitation (Friedrich et al., 2020). In reality, natural snowfall may contribute significantly. It is difficult to quantitatively separate the precipitation attributed to cloud seeding from natural precipitation. Nevertheless, unambiguous seeding signatures in precipitating clouds can still be useful in studying the chain of physics of cloud seeding.

- The 1D model does not thermodynamically constrain the LWC available for glaciogenic seeding. Under limited LWC, a

515   larger AgI concentration may reduce the radar reflectivity enhancement, because more, but smaller ice crystals will form, compared lower AgI concentration. Such constraint is captured in a 3D model.

In short, the results shown in this study deepen our understanding of the relationships between AgI particle concentration and Ze under different cloud conditions. The parameterization has limitations, but it can be useful in seeding operations to provide

520   a quick estimation of how much AgI particle concentration is needed to obtain an unambiguous seeding signature.

Data availability

The WRF model is available on https://www2.mmm.ucar.edu/wrf/users/download/get_source.html (NCAR MMM, 2023). The sounding data, radar data and ice growth model are available on https://doi.org/10.5281/zenodo.12793527 (Yang, 2024).

Author contributions

JY, JL, and MC conducted the numerical simulations. JY, JL and XJ evaluated and analyzed the model results. JY and XJ prepared the paper. HH provided the data of radar measurements. YY, BG, ZW, YL and BC provided inputs on the method and analysis. All the authors provided significant feedback on the paper.

Competing interests

The contact author has declared that none of the authors has any competing interests.

Acknowledgements

This work was supported by the National K&D Program of China (2023YFC3007600), the National Natural Science Foundation of China (42230604), and the CMA Key Innovation Team Support Project (CMA2022ZD10). We acknowledge the High Performance Computing Center of Nanjing University of Information Science & Technology for their support of this work. We appreciate the editor and reviewers for their insightful comments and suggestions.

References

Breed, D., Rasmussen, R., Weeks, C., Boe, B., and Deshler, T.: Evaluating winter orographic cloud seeding: Design of the Wyoming Weather Modification Pilot Project (WWMPP). J. Appl. Meteor. Climatol., 53, 282–299, https://doi.org/10.1175/JAMC-D-13-0128.1, 2014.

Bailey, M. P., and Hallett, J.: A comprehensive habit diagram for atmospheric ice crystals: Confirmation from the laboratory, AIRS II, and other field studies. J. Atmos. Sci., 66, 2888–2899, https:// doi.org/10.1175/2009JAS2883.1, 2009.

Caro, D., Wobrock, W., Flossmann, A. I., and Chaumerliac, N.: A two-moment parameterization of aerosol nucleation and impaction scavenging for a warm cloud microphysics: Description and results from a two-dimensional simulation. Atmos. Res., 70, 171–208, 2004.

Chen, J.-P., and Lamb, D.: The theoretical basis for the parameterization of ice crystal habits: Growth by vapor deposition. J. Atmos. Sci., 51, 1206–1222, doi:10.1175/1520-0469(1994)051<1206:TTBFTP>2.0.CO;2, 1994.

Chu, X., Xue, L., Geerts, B., Rasmussen, R., and Breed, D.: A case study of radar observations and WRF LES simulations of the impact of ground-based glaciogenic seeding on orographic clouds and precipitation. Part I: Observations and model validations. J. Appl. Meteor. Climatol., 53, 2264–2286, https://doi.org/10.1175/JAMC-D-14-0017.1, 2014.

DeMott, P. J.: Quantitative descriptions of ice formation mechanisms of silver iodide-type aerosols, Atmospheric Research, 38, 1, 63-99,https://doi.org/10.1016/0169-8095(94)00088-U, 1995.

Deshler, T., Reynolds, D. W., and Huggins, A. W.: Physical response of winter orographic clouds over the Sierra Nevada to airborne seeding using dry ice or silver iodide. J. Appl. Meteor., 29, 288–330, https://doi.org/10.1175/1520-0450(1990) 029,0288:PROWOC.2.0.CO;2, 1990.

555 Dong, X., Zhao, C., Yang, Y., Wang, Y., Sun, Y., and Fan, R.: Distinct change of supercooled liquid cloud properties by aerosols from an aircraft-based seeding experiment. Earth and Space Science, 7, e2020EA001196. https://doi.org/ 10.1029/2020EA001196, 2020.

Dong, X. B., Zhao, C. F., Huang, Z. C., et al: Increase of precipitation by cloud seeding observed from a case study in November 2020 over Shijiazhuang, China. Atmos. Res., 262: 105766. doi:10.1016/j. atmosres.2021.105766, 2021.

560 French, J. R., and Coauthors: Precipitation formation from orographic cloud seeding. Proc. Natl. Acad. Sci. USA, 115, 1168–1173, https://doi.org/10.1073/pnas.1716995115, 2018.

Friedrich, K., and Coauthors: Quantifying snowfall from orographic cloud seeding. Proc. Natl. Acad. Sci. USA, 117, 5190–5195, https://doi.org/10.1073/pnas.1917204117, 2020.

Friedrich, K., French, J., Tessendorf, S., Hatt, M., Weeks, C., Rauber, R., Geerts, B., Xue, L., Rasmussen, R., Blestrud, D.,

565 Kunkel, M., Dawson, N., and Parkinson, S.: Microphysical characteristics and evolution of seeded orographic clouds. J. Appl. Meteor. Climat., 60, 909-934, https://doi.org/10.1175/JAMC-D-20-0206.1, 2021.

Fukuta, N., and Takahashi, T. The growth of atmospheric ice crystals: A summary of findings in vertical supercooled cloud tunnel studies. J. Atmos. Sci., 56, 1963–1979, https://doi.org/10.1175/ 1520-0469(1999)056,1963:TGOAIC.2.0.CO;2, 1999.

Geerts, B., and Coauthors: The AgI Seeding Cloud Impact Investigation (ASCII) campaign 2012: Overview and preliminary

570 results. J. Wea. Modif., 45, 24–43, https://doi.org/10. 54782/jwm.v45i1.121, 2013.

Geerts, B., and Rauber, R. M.: Glaciogenic Seeding of Cold-Season Orographic Clouds to Enhance Precipitation: Status and Prospects. Bull. Amer. Meteor. Soc., 103, E2302–E2314, https://doi.org/10.1175/BAMS-D-21-0279.1, 2022.

Heymsfield, A. J.: A comparative study of the rates of development of potential graupel and hail embryos in High Plains storms. J. Atmos. Sci., 39, 2867–2897, doi:10.1175/1520-0469(1982)039<2867:ACSOTR>2.0.CO;2, 1982.

575 Heymsfield, A. J., and Westbrook, C. D.: Advances in the estimation of ice particle fall speeds using laboratory and field measurements. J. Atmos. Sci., 67, 2469–2482, doi:10.1175/2010JAS3379.1, 2010.

Hobbs, P. V., Lyons, J. H., Locatelli, J. D., Biswas, K. R., Radke, L. F., Weiss Sr., R. R., and Rangno, A. L.: Radar detection of cloud-seeding effects. Science, 213, 1250–1252, https://doi.org/10.1126/science.213.4513.1250, 1981.

Huggins, A. W., 2007: Another wintertime cloud seeding case study with strong evidence of seeding effects. J. Wea. Modif.,

580 39, 9–36.

Jiménez, P. A., Dudhia, J., González-Rouco, J. F., Navarro, J., Montávez, J. P., and García-Bustamante, E.: A Revised Scheme for the WRF Surface Layer Formulation, Mon. Weather Rev., 140, 898–918, https://doi.org/10.1175/MWR-D-11-00056.1, 2012.

Hua, S., Chen, B., He, H., Chen, Y., Liu, X., Yang, J.: Numerical simulation of the cloud seeding operation of a convective

585 rainfall event occurred in Beijing, Atmos. Res., 304, 107386, https://doi.org/10.1016/j.atmosres.2024.107386.

Jing, X., and Geerts, B.: Dual-polarization radar data analysis of the impact of ground-based glaciogenic seeding on winter orographic clouds. Part II: Convective clouds. J. Appl. Meteor. Climatol., 54, 2099–2117, https://doi.org/10.1175/JAMC-D-15-0056.1, 2015.

590 Jing, X, Geerts, B., Friedrich, K., and Pokharel, B.: Dual-polarization radar data analysis of the impact of ground-based glaciogenic seeding on winter orographic clouds. Part I: Mostly stratiform clouds. J. Appl. Meteor. Climatol., 54, 1944–1969, https://doi.org/10.1175/JAMC-D-14-0257.1, 2015.

Jing, X., Geerts, B., and Boe, B.: The Extra-Area Effect of Orographic Cloud Seeding: Observational Evidence of Precipitation Enhancement Downwind of the Target Mountain. J. Appl. Meteor. Climatol., 55, 1409–1424, https://doi.org/10.1175/JAMC-D-15-0188.1, 2016.

595 Khain, A., Pokrovsky, A., Pinsky, M., Seifert, A., and Phillips, V.: Simulation of Effects of Atmospheric Aerosols on Deep Turbulent Convective Clouds Using a Spectral Microphysics Mixed-Phase Cumulus Cloud Model. Part I: Model Description and Possible Applications, J. Atmos. Sci., 61, 2963–2982, https://doi.org/10.1175/JAS-3350.1, 2004.

Korolev, A., and Field, P. R.: The Effect of Dynamics on Mixed-Phase Clouds: Theoretical Considerations. J. Atmos. Sci., 65, 66–86, https://doi.org/10.1175/2007JAS2355.1, 2008.

600 Mace, G. Ackerman, G., T. P., Minnis, P., and Young, D. F.: Cirrus layer microphysical properties derived from surface-based millimeter radar and infrared interferometer data. J. Geophys. Res., 103, 23 207–23 216, doi:10.1029/98JD02117, 1998.

Mason, B. J.: The growth of ice crystals in a supercooled water cloud. Quart. J. Roy. Meteor. Soc., 79, 104–111, doi:10.1002/qj.49707933909, 1953.

Manton, M. J., and Warren, L.: A confirmatory snowfall enhancement project in the snowy mountains of Australia. Part II: 605 Primary and associated analyses. J. Appl. Meteor. Climatol., 50, 1448–1458, https://doi.org/10.1175/2011JA MC2660.1, 2011.

Meyers, M. P., DeMott, P. J., and Cotton, W. R.: A comparison of seeded and nonseeded orographic cloud simulations with an explicit cloud model. J. Appl. Meteor., 34, 834–846, 1995.

Mlawer, E. J., Taubman, S. J., Brown, P. D., Iacono, M. J., and Clough, S. A.: Radiative transfer for inhomogeneous atmospheres: RRTM, a validated correlated-k model for the longwave, J. Geophys. Res.-Atmos., 102, 16663–16682, 610 https://doi.org/10.1029/97JD00237, 1997.

NCAR MMM: Weather Research & Forecasting Model (WRF), UCAR [software], https://www2.mmm.ucar.edu/wrf/users/download/get_source.html (last access: 15 March 2023), 2023.

Pinsky, M., Khain, A., and Korolev, A.: Theoretical Analysis of Liquid–Ice Interaction in the Unsaturated Environment with Application to the Problem of Homogeneous Mixing. J. Atmos. Sci., 75, 1045–1062, https://doi.org/10.1175/JAS-D-17-0228.1, 615 2018.

Pokharel, B., Geerts, B., and Jing, X.: The impact of ground-based glaciogenic seeding on orographic clouds and precipitation: A multisensor case study. J. Appl. Meteor. Climatol., 53, 890–909, https://doi.org/10.1175/JAMC-D-13-0290.1, 2014.

Rauber, R. M.,, and Coauthors: Wintertime orographic cloud seeding}A review. J. Appl. Meteor. Climatol., 58, 2117–2140, https://doi.org/ 10.1175/JAMC-D-18-0341.1, 2019.

620 Qu, Y., Chen, B., Ming, J., Lynn, B. H., & Yang, M.-J.: Aerosol impacts on the structure, intensity, and precipitation of the landfalling Typhoon Saomai (2006). Journal of Geophysical Research: Atmospheres, 122. https://doi.org/10.1002/2017jd027151, 2017.

Rasmussen, R. M., and Coauthors: Evaluation of the Wyoming Weather Modification Pilot Project (WWMPP) using two approaches: Traditional statistics and ensemble modeling. J. Appl. Meteor. Climatol., 57, 2639–2660, https://doi.org/10.

625 1175/JAMC-D-17-0335.1, 2018.

Takahashi, T., Endoh, T., Wakahama, G., and Fukuta, N.: Vapor diffusional growth of free-falling snow crystals between -3ºC and -23ºC. J. Meteor. Soc. Japan, 69, 15–30, 1991.

Tessendorf, S. A., and Coauthors: Transformational approach to winter orographic weather modification research: The SNOWIE project. Bull. Amer. Meteor. Soc., 100, 71–92, https://doi.org/10.1175/BAMS-D-17-0152.1, 2019.

630 Tewari, M., Chen, F., Wang, W., Dudhia, J., LeMone, M. A., Mitchell, K., Ek, M., Gayno, G., Wegiel, J., and Cuenca, R. H.: Implementation and verification of the unified NOAH land surface model in the WRF model, 20th Conference on Weather Analysis and Forecasting/16th Conference on Numerical Weather Prediction, 12–16 January 2004, American Meteorological Society, Seattle, WA, US, 11–15, 2004.

Wallace, J. M., and Hobbs, P.V.: Atmospheric Science, An Introductory Survey (International Geophysics). Second Edition,

635 Academic Press, 504pp, 2006.

Wang, J., Yue, Z., Rosenfeld, D., Zhang, L., Zhu, Y., Da,i J., Yu, X., and Li, J.: The evolution of an AgI cloud-seeding track in central China as seen by a combination of radar, satellite, and disdrometer observations. J. Geophys. Res. Atmos., 126, e2020JD033914, https://doi.org/10.1029/2020JD033914, 2021.

Wang, X., Dong, X., Yang, J., et al.: Analysis of Physical Response to Cold Cloud Seeding over North China in Winter Based

640 on Multisource Observations. Chinese Journal of Atmospheric Sciences (in Chinese), 48, 1−14. https://doi.org/10.3878/j.issn.1006-9895.2311.23061, 2024.

Xue, L., and Coauthors: Implementation of a silver iodide cloud seeding parameterization in WRF. Part I: Model description and idealized 2D sensitivity tests. J. Appl. Meteor. Climatol., 52, 1433–1457, https://doi.org/10.1175/JAMC-D-12-0148.1, 2013a.

645 Xue, L., Tessendorf, S. A., Nelson, E., Rasmussen, R., Breed, D., Parkinson, S., Holbrook, P., and Blestrud, D.: Implementation of a silver iodide cloud seeding parameterization in WRF. Part II: 3D simulations of actual seeding events and sensitivity tests. J. Appl. Meteor. Climatol., 52, 1458–1476, https://doi.org/10.1175/JAMC-D-12-0149.1, 2013b.

Xue, L., and Coauthors: Comparison between Observed and Simulated AgI Seeding Impacts in a Well-Observed Case from the SNOWIE Field Program. J. Appl. Meteor. Climatol., 61, 345–367, https://doi.org/10.1175/JAMC-D-21-0103.1, 2022.

650 Yue, Z., Yu, X., Liu, G., et al. Effect evaluation of an operational precipitation enhancement in cold clouds by aircraft. Acta Meteorologica Sinica (in Chinese), 79, 853−863. doi:10.11676/qxxb2021.051, 2021.

Yang, J., Wang, Z., Heymsfield, A., and Luo, T.: Liquid-ice mass partition in tropical maritime convective clouds, J. Atmos. Sci., 73, 4959–4978, https://doi.org/10.1175/JAS-D-15-0145.1, 2016a.

Yang, J., Wang, Z., Heymsfield, A., French, J.: Characteristics of Vertical Air Motion in Isolated Convective Clouds. Atmos.

655 Chem. Phys., 16, 10159–10173, 2016b.

Yang, J., Qin, Z., Deng, Y., Chen, M., Jing, X., Yin, Y., et al.: On the cluster scales of hydrometeors in mixed-phase stratiform clouds. Geophysical Research Letters, 51, e2024GL108166. https://doi. org/10.1029/2024GL108166, 2024.

Yang, J.: Estimating AgI concentration [Dataset]. Zenodo. https://doi.org/10.5281/zenodo.12793527, 2024

Zaremba, T. J., Rauber, R. M., Girolamo, L. D., Loveridge, J. R., and McFarquhar, G. M.: On the Radar Detection of Cloud

660 Seeding Effects in Wintertime Orographic Cloud Systems. J. Appl. Meteor. Climatol., 63, 27–45, https://doi.org/10.1175/JAMC-D-22-0154.1, 2024.

Zhang, D., Wang, Z., Heymsfield, A., Fan, J., and Luo, T.: Ice Concentration Retrieval in Stratiform Mixed-Phase Clouds Using Cloud Radar Reflectivity Measurements and 1D Ice Growth Model Simulations. J. Atmos. Sci., 71, 3613–3635, https://doi.org/10.1175/JAS-D-13-0354.1, 2014.

665